HHS Public Access

Author manuscript

Mol Imaging Biol. Author manuscript; available in PMC 2024 April 01.

Published in final edited form as:

Mol Imaging Biol. 2023 April ; 25(2): 401–412. doi:10.1007/s11307-022-01770-w.

Omniparticle contrast agent for multimodal imaging: synthesis and characterization in an animal model

Neil Robertson[1,2], **Lorenzo Sempere**[1,2], **Elizabeth Kenyon**[1,2], **Christiane Mallet**[2,5], **Kylie Smith**[3,5], **Jeremy Hix**[2,5], **Alan Halim**[1], **Jinda Fan**[2,3,4,5], **Anna Moore**[1,2,*]

[1]Precision Health Program, Michigan State University, 766 Service Road, East Lansing, MI 48824 USA

[2]Department of Radiology, College of Human Medicine, Michigan State University, 766 Service Road, East Lansing, MI 48824, USA

[3]Department of Biomedical Engineering, College of Engineering, Michigan State University, 766 Service Road, East Lansing, MI 48824, USA

[4]Department of Chemistry, College of Natural Sciences, Michigan State University, 578 S Shaw Lane, East Lansing MI 48824, USA

[5]Institute for Quantitative Health Science and Engineering, Michigan State University, 775 Woodlot Drive, East Lansing, MI 48824, USA

Abstract

Purpose: Individual imaging modalities have certain advantages, but each suffers from drawbacks that other modalities may overcome. The goal of this study was to create a novel contrast agent suitable for various imaging modalities that after a single administration can bridge and strengthen the collaboration between the research fields as well as enrich the information obtained from any one modality.

Procedures: The contrast agent platform is based on dextran coated iron oxide nanoparticles (for MRI and MPI) and synthesized using a modified co-precipitation method, followed by a series of conjugation steps with a fluorophore (for fluorescence and photoacoustic imaging), thyroxine (for CT imaging) and chelators for radioisotope labeling (for PET imaging). The fully conjugated agent was then tested *in vitro* in cell uptake, viability and phantom studies and *in vivo* in a model of intraductal injection and in a tumor model.

Results: The agent was synthesized, characterized and tested *in vitro* where it showed the ability to produce a signal on MRI/MPI/FL/PA/CT and PET images. Studies in cells showed the expected concentration-dependent uptake of the agent without noticeable toxicity. *In vivo*

*Corresponding author: Anna Moore, moorea57@msu.edu.

Authors' contributions: N.R. designed and synthesized of the compound, wrote the draft of the manuscript; L.S. contributed to the concept, designed the animal model, contributed to data acquisition and analysis, revising the manuscript, and financial support of the study; E.K. contributed to the design of the animal model, data acquisition and analysis; C.M., K.S. and J.X. contribution to in vitro and in vivo imaging, data acquisition and analysis; A.H. assisted with cellular work; J.F. contributed to synthesis, radiolabeling, data acquisition and analysis; A.M contributed to the concept, revision of the manuscript, data analysis and financial support of the study.

Ethics Approval: Not applicable.

Conflict of Interest: Authors declare no conflict of interest

studies demonstrated localization of the agent to the ductal tree in mice after intraductal injection with different degree of resolution, with CT being the best for this particular application. In a model of injected labeled tumor cells, the agent produced a signal with all modalities and showed persistence in tumor cells confirmed by histology.

Conclusions: A fully functional omniparticle contrast agent was synthesized and tested *in vitro* and *in vivo* in two animal models. Results shown here point to the generation of a potent signal in all modalities tested without detrimental toxicity. Future use of this agent includes its exploration in various models of human disease including image-guided diagnostic and therapeutic applications.

Introduction

Imaging is a powerful and rapidly growing field of biomedical research, proven indispensable for the early detection, diagnosis and treatment of various cancer types [1–9] and tracking cells of interest *in vivo* [10–13]. Whether in the clinical or preclinical setting, the concept of 'seeing is believing' has significant implications. Clinicians and researchers alike prefer direct observation of disease over indirect study, as seeing through conventional imaging modalities greatly enhances the assessment of treatment management, disease stage and localization [5]. While biopsy might seem to be the current most direct method of accessing the disease, the procedure is invasive and suffers from lack of representation due to disease heterogeneity and the necessity to study the tissue outside of the living system. As a result, biomedical imaging has become a necessary tool for non-invasive disease visualization.

While anatomical imaging can provide general information about spatial and structural details, contrast agents can deliver specific information about localization of the lesion [14–16], the stage of the disease [17–18] and response to treatment [17, 19–20]. Preclinical development of novel imaging agents and modalities is necessary as it helps to drive the way diseases are treated and diagnosed, and link interdisciplinary approaches to gain complementary information about tissue of interest [21]. While certain advantages are obvious, each individual imaging modality suffers from a different drawback that other modalities may overcome (reviewed in [22]). Bioluminescence is one of the preclinical tools being vastly used for biomedical research, however it suffers from depth attenuation and is not available in a clinical setting [23]. In contrast, positron emission tomography (PET) do not suffer from depth attenuation, though PET utilizes ionizing radiation and has a relatively short half-life. Magnetic resonance imaging (MRI) provides an indirect measurement of the contrast agent used and has low sensitivity but provides a better soft tissue contrast compared to other modalities [24]. A newer imaging modality known as magnetic particle imaging (MPI) provides a direct measurement of a contrast agents' concentration, has high resolution but low availability of contrast agents [9], however, the availability of instrumentation limits its application. In addition, it is not clinically available as of today. As a result, researchers often rely on various formulations of contrast agents in an attempt to co-register the signal with different modalities, but the references for each may be significantly different.

To overcome these individual limitations, we sought to combine the agents that would be used for multiple imaging modalities into a single contrast agent. Interest to combine modalities has been explored to some extent for MRI/FL [25–30], MRI/MPI [31] and MPI/CT [32]. Our proposed contrast agent, however, combines multiple imaging modalities such as magnetic resonance imaging (MRI), magnetic particle imaging (MPI), computed tomography (CT), fluorescence (FL), photoacoustic (PA), and positron emission tomography (PET) into a single nanoparticle formulation (termed omniparticle). The multimodal aspect may help bridge specific gaps in information lost with any single imaging modality and aid in the enhanced collaboration between the various imaging fields. Our omniparticle contrast agent was achieved through a superparamagnetic iron oxide core (MRI and MPI) functionalized with a modified dextran coating with a fluorophore (FL/PA/US), chelating agent (PET) and thyroxine (CT) (Fig. 1a).

Here we report on the synthesis and characterization of the agent, and present in vitro and in vivo data demonstrating the utility of the agent in a model system of intraductal (ID) delivery into the murine mammary gland and for imaging of labeled tumor cells. There is a growing literature on preclinical [33–38] and clinical [39–40] applications of intraductal procedures for diagnostic, therapeutic and breast cancer preventive purposes including from our laboratory. Part of the requirement of this technique is the need to image the full ductal tree network to understand what regions were correctly treated and if there were any blockages or incomplete filling of the tree during the ablation [38, 41]. In this work we used a model of ID injection to test the utility of our omniparticles for monitoring the delivery to the ductal tree.

Cell tracking in vivo requires strategies for labeling cells with contrast agents [42–44]. The ability to monitor efficiently labeled cells provides information about functional status of cells in vivo in various settings. Here, we demonstrate the ability of our agent to efficiently label tumor cells followed by imaging of these cells after implantation in mice using various imaging modalities.

By providing a universal tool to the biomedical imaging field, we hope to corroborate registered signals and potentially enhance the information acquired in the clinic.

Materials and Methods

Magnetic nanoparticle (MNP) synthesis:

The iron oxide nanoparticles were synthesized with a newly adapted co-precipitation technique fully described in Electronic Supplementary Materials (see ESM). Hydrodynamic diameter and zeta potential measurements were performed using a Zetasizer particle analyzer (Malvern). The Transmission Electron Microscopy (TEM) images were captured using an ultrahigh resolution JEM-2200FS Field Emission Electron Microscope (Jeol). T1/T2 relaxation times were measured using Bruker Minispec MQ20 0.47T.

Fluorophore conjugation:

After amination and sonication, the nanoparticles were conjugated with a Cy5.5-NHS dye (Lumiprobe) to allow for fluorescent/photoacoustic imaging. Briefly, 100 μL of the dye (10

mM stock) suspended in DMSO was mixed with 400 μL of a sodium citrate buffer (20 mM Na-Citrate, 150 mM NaCl, pH 8.4) to dissolve fully. Next, 1.1 mL of the freshly prepared nanoparticles was added to this mixture and placed on a rotor overnight at room temperature. After the conjugation was complete, unconjugated dye was removed with a Sephadex G-25 PD-10 column (GE Healthcare) against the sodium citrate buffer pH 8.4.

PET chelator attachment and Cu-64 labeling:

Similar to the fluorophore conjugation, a DOTA-NHS chelator (Macrocyclics; Plano, Texas USA) was next conjugated to the nanoparticle construct to allow for PET imaging. Details on the conjugation are presented in Electronic Supplementary Materials.

CT agent attachment:

To achieve imaging with CT a small iodine-binding molecule thyroxine (T4, 3-[4-(4-Hydroxy-3,5-diiodophenoxy)-3,5-diiodophenyl]-L-alanine, Sigma-Aldrich) was attached to the dextran coating. Thyroxine is a naturally occurring thyroid hormone, carrying four covalently bound iodine molecules, and therefore was considered a perfect choice to further enhance the omniparticle contrast agents' capabilities. Details on the conjugation are presented in Electronic Supplementary Materials.

For phantom imaging, we prepared the nanoparticle construct at 200 μg of Fe/mL labeled with 400 μCi of Cu-64.

In vitro studies with cells—To test the cellular uptake, increasing concentrations (0–200μg/ml) of fully functionalized contrast agent containing MRI/MPI/FL/PA/CT and PET capabilities were incubated with MDA-MB-231 human breast cancer cells for 2 hrs. After incubation cells were washed and imaged using IVIS Spectrum (Perkin Elmer). To quantitate iron uptake, cells were lysed and analyzed using Total Iron Reagent Kit (Pointe Scientific).

Cellular toxicity was analyzed in MDA-MB-231 cells after incubation with the increasing concentrations of the agent (0–200μg/ml) for 2 hrs using MTT Cell Viability Assay (Invitrogen).

Cell phantoms were produced after incubation of 9×10^5 cells with Cu-64-labeled agent (200μg/ml, 2.32 μCi final activity) for 2 hrs following imaging with multiple modalities (CT, MPI, FL, PA and PET/MRI) as described below.

In vivo animal models

Model of intraductal injection (ID): Anesthetized FVB/NJ female mice (9–12 weeks old, n = 3–5 per modality; Jackson Labs; jax.org stock 001800) were injected intraductally into glands #4 and/or #9 as described [45] with the contrast agent suspended in either a PBS or EtOH (40 μL of a 7:3 mixture of 70% ethanol:contrast agent mixture, 200 μgFe). EtOH was used in certain images to mimic future ablation studies. Visual inspection of the ductal tree after ID injection showed distinct branches of the tree and was performed for the injection quality control (Supplemental Fig. 1, see ESM). For *in vivo* imaging, mice were imaged

before and immediately after ID injection with multiple modalities (CT, MPI, FL, PA and PET/MRI) as described below.

Tumor model: Anesthetized nu/nu mice (n=5, Jackson Labs) were injected with luciferase-expressing 1.4×10^5 MDA-MB-231 human breast cancer cells labeled with omniparticles. Prior to injection cells were labeled by incubation with 400μg/ml of the agent for 2 hour. Labeled cells were injected in the 3rd mammary fat pad at 3.08+/−1.3μCi/injection. Unlabeled cells were injected in the contralateral 8th fad pad. Animals were image pre- and postcontrast with multiple modalities (CT, MPI, FL, PA and PET/MRI) as described below.

All experiments were conducted under protocols approved by Institutional Animal Care and Use Committee at Michigan State University.

Fluorescence imaging *in vitro*/*in vivo*/*ex vivo*:

Fluorescence imaging with the omniparticle phantom or cell phantom, *in vivo* and *ex vivo* imaging was performed in Cy5.5 fluorophore channel (ex. 676 nm, em. 705 nm) using a whole body animal scanner (IVIS Spectrum, Perkin Elmer). For *in vivo* imaging, animals were imaged before and immediately post injection of the contrast agent for the ductal tree model. Animals injected with labeled cells were imaged immediately after and 5 days after the injection of the cells.

For *ex vivo* fluorescence microscopy, the ductal tree or mammary fat pad tissues were collected, frozen and sectioned prior to imaging with an Aperio Versa whole tissue-slide imaging system (Leica Biosystems). Tissues were stained with H&E staining and fluorescence microscopy was used to validate the agent accumulation in the ductal epithelial cells or in tumor cells.

Photoacoustic (PA) imaging *in vitro*/*in vivo*:

Phantom photoacoustic imaging was performed with the same phantoms as FL imaging. Tubes with omniparticles or labeled cells resuspended in a 2% soft agar were placed in the multispectral optoacoustic tomography (MSOT) scanner (MSOT InVision 128, iTheraMedical). All tubes were imaged at the same time in the same manner. The following parameters were used: nine excitation wavelengths (660, 670, 680, 700, 730, 760, 800, 850, 875(nm)); ten frames averaged per wavelength. Background wavelength was determined to be 875 nm by the iThera MSOT inVision 128 and Cy5.5 was probed between 660–710 nm, as determined by the instrument. Linear regression algorithm was used for Multi-Spectral Processing (MSP) analysis and image reconstruction with 100μm reconstruction resolution. The same scan parameters were used for *in vivo* imaging described below.

In vivo PA imaging was performed in mice before and immediately after ID injection of the contrast agent or labeled tumor cell injections. PA acquisition ran for roughly 10 min at 0.5 mm steps across a 20 mm section of the lower abdominal region.

Computed Tomography (CT) imaging *in vitrolin vivo*:

Phantom CT imaging was performed with the same phantoms as FL imaging on a Quantum GX microCT scanner (Perkin Elmer). The following image acquisition scan parameters were standardized and used at each scan (in vitro and in vivo): 90 kVp/88 μA; field of view (FOV), 36 mm; number of slices 512; slice thickness, 72 μm; voxel resolution, 72 μm^3. microCT image rendering, segmentation and analysis of whole body or individual gland were performed using Caliper AnalyzeDirect©, v12.0 (Biomedical Imaging Resource, Mayo Clinic, Rochester, MN).

Magnetic particle imaging (MPI) *in vitrolin vivo*:

Phantom MPI imaging was performed with the same phantoms as FL imaging on a Momentum Magnetic Particle Imager (MPI, Magnetic Insight). For in vivo and phantom imaging, the following parameters were used: for 2D scans FOV of 4 cm x 6 cm, a 6 T/m selection field gradient, a drive field strength of 20 mT peak amplitude, a 45.0 kHz drive frequency, and an acquisition time of ~ 10 seconds. 3D scans were acquired with a FOV of 6 cm x 6 cm x 6 cm, 55 projections, acquisition time of ~ 10 minutes, with a total imaging time including reconstruction of ~ 35 minutes. Gradient strength, drive field strength, and drive frequency were the same.

Magnetic Resonance Imaging (MRI)/Positron Emission Tomography (PET) *in vitrolin vivo*:

Phantom MR imaging studies of various nanoparticle formulations were carried out on a 7T BioSpec 70/30 MRI (Bruker). The formulations were as follows: 1) the MNP core (Fe_3O_4) synthesized as described previously [30], 2) the MNP core (Fe_3O_4) synthesized as described above conjugated to a fluorophore (Cy5.5), 3) the same nanoparticle core (Fe_3O_4) conjugated to a fluorophore and thyroxine, 4) the nanoparticle core completely oxidized to Fe_2O_3 with 5% H_2O_2 and 5) water. The imaging protocol consisted of T2-weighted spin echo pulse sequences with the following parameters: spin echo repetition time/echo time = 800/7,11,15,19, 23, 27, 31, 35; field of view (FOV) = 32 × 34 μm^2; matrix size = 128 × 128 pixels; slice thickness = 0.5 mm; in plane resolution = 250 × 250 μm^2. Images were reconstructed and analyzed by Paravision 360 software (Bruker). T2 maps were constructed according to established protocol by fitting T2 readings for each of the eight echo times to a standard exponential decay curve.

For phantom PET imaging, an omniparticle solution containing (400 μCi) was placed in the BioSpec scanner with PET insert. Acquisition time for PET imaging was 30 minutes. A maximum likelihood expectation maximization (MLEM) algorithm was used for PET image reconstruction at 0.5 mm^3 voxel size with decay correction, scatter correction, and randoms correction included. The corrected PET scans were geometrically co-registered to the MR scans in ParaVision acquisition software and exported to PMOD 4.2 (PMOD Technologies, LLC) for figure generation.

In vivo MR of the ductal tree injections was performed using the parameters described above with 12 slices across the lower abdominal region of the mice to capture the wrapping of the ductal tree. The imaging protocol was the same as described above. Images were reconstructed and analyzed by Paravision 360 software. Animal orientation

was coronal, with geometry registered for all PET/MR scans. *In vivo* PET acquisition occurred simultaneously with MR imaging and ran for 30 minutes of acquisition time.

Upon the completion of the imaging session ductal trees were excised and processed for autoradiography as described below.

MR imaging of labeled cell phantoms containing 2.32 μCi of Cu-64 and *in vivo* MR imaging of injected labeled tumor cells was performed using a T1 FLASH (T_E/T_R = 5/500 ms, 3 averages, 1 repetition, 0.25 mm voxel, 0.474 mm slice thickness, 40 × 40 mm field of view, scan time 3 min). Simultaneously, PET data was acquired in a single 30-minute bin and geometrically co-registered to the T1 FLASH scans in ParaVision acquisition software and exported to PMOD 4.2 (PMOD Technologies, LLC) for figure generation.

Autoradiography:

Ex vivo autoradiography was accomplished by incubating surgically removed fat pads immediately post *in vivo* PET imaging with a reusable storage phosphorescence screen capable of detecting beta decay (Amersham Typhoon Biomolecular Imager, GE Healthcare). Incubation times varied from 30 seconds to 1 hour to obtain appropriate saturation levels.

Results

Synthesis and characterization of the omniparticle contrast agent.

The omniparticle agent was created with a co-precipitation method and composed of an iron oxide (Fe_3O_4) core with a coating of dextran (Fig. 1b). The use of the dextran coating was pursued for two reasons: 1) it allows for functionalization of the nanoparticle construct after an initial amination process and 2) our laboratory and others have found excellent biocompatibility and long circulation time *in vivo* for dextran-coated nanoparticles [29–30, 46–49]. Transmission Electron Microscopy (TEM) showed the as-prepared unconjugated iron oxide nanoparticle core with a diameter between 15–20 nm with about 5nm dextran coating (Fig. 1c) while dynamic light scattering (DLS) showed a hydrodynamic diameter of 30.67 +/− 1.53 nm. Slightly higher number obtained with DLS is mostly due to the dehydration process used for TEM imaging. Zeta-potential of the construct prior to conjugation was +20.45 +/− 1.65 mV, while R1/R2 relaxivities were 19.64 and 194.837 $mM^{-1}s^{-1}$ respectively. The nanoparticles were then modified with a Cy5.5 fluorophore through NHS-ester chemistry to attain fluorescent and photoacoustic imaging capabilities. The average number of fluorophores per MNP was 7. To allow for PET imaging, the respective chelator with an NHS-ester was utilized. Simple mixing of the nanoparticle construct and DOTA chelator selected for PET imaging under slightly basic conditions allowed for the conjugation of multiple chelators. The average number of chelators per particle was found to be 10.

To obtain CT imaging capabilities, the use of thyroxine (or T4) was explored. As a precursor to a naturally occurring growth hormone, and containing four covalently bound iodine molecules, it was considered an excellent fit for obtaining a multimodal nanoparticle complex. The attachment was carried out by parallel conjugation of an SPDP linker to the nanoparticles and conjugation of an SMPH linker to T4, prior to the mixing of them

together. Varying the amount of T4 had the largest impact on stability and solubility of the contrast agent, with optimal conditions found to be between 5–10 T4 molecules per particle. The zeta-potential of the construct post conjugation was found to be 15.02 +/− 2.41 mV.

After characterization of the agent, we set to perform phantom imaging. First, we performed two dimensional MPI that demonstrated a robust signal (Fig. 2a, image overlaid with signal intensity for clarification). Serial dilutions of the agent showed linearity of the signal on MPI images (R^2=0.9955; Supplemental Fig. 2 (see ESM)). T2-weighted MR imaging was also performed on various nanoparticle formulations to test the relaxivity of the constructs (Fig. 2b). Here we compared our novel omniparticle contrast agent to our previously reported agent with MRI-active core [30, 50] and control construct that lost T2 imaging potential due to oxidation with 5% H_2O_2. The novel construct formulation showed similar attenuation potential to that of our previously synthesized nanoparticle constructs ((1) in Fig 2b), with a smaller average core size that were successfully used as MR contrast agents *in vivo* [30, 50].

After imaging with the core modalities, we next performed imaging of the conjugated moieties. The strong signal measured in fluorescence mode originated from the phantoms due to the presence of a Cy5.5 optical dye (ex. 675, em. 705) (Fig. 2c). Similarly, the phantoms in PA imaging showed robust signal generation when compared to the blank water phantom (Fig. 2d). We also performed PET imaging after chelation of Cu-64 with DOTA that showed strong signal originating from the phantom (Fig. 2e). All angles used in this modality along with the maximum intensity projection are shown in Supplemental Fig. 3 (see ESM). We next tested phantoms of our construct using CT, to gauge the strength of T4 incorporation in the agent. Fig. 2f shows the 3D view of the contrast agent phantom with CT imaging.

In vitro studies with the omniparticle contrast agent.

Since one of the goals is to use the synthesized omniparticles for cancer imaging, we performed initial in vitro studies in the MDA-MB-231 breast cancer cell line. Qualitatively, we observed concentration-dependent increase of the signal in the Cy5.5 channel (Fig. 3a). Quantitatively, the uptake determined by iron assay ranged from 10–94 pg Fe/cell (Fig. 3b). Next, we tested toxicity of the agent in a cellular viability assay using the same MDA-MB-231 cell line. We observed virtually no effect on cell viability similar to what we found with other iron oxide-based agents [51] (Fig. 3c).

In addition, after labeling cells with Cu-64-labeled agent they were imaged in a cell phantom with all imaging modalities (Fig. 3d). Iron accumulation as well as the signals originating from conjugating moieties were readily detectable. The amount of iron in cell the phantom calculated by MPI was 67.9+/−2.2 μg, which was slightly different from the uptake studies (84.6+/−4.3 μg).

In vivo studies

Model of intraductal injection.: After initial in vitro studies we performed in vivo testing of the agent in the model of ID delivery. To this end, we injected the omniparticle contrast agent into the ductal trees of mice and imaged them using various modalities. As seen in

Fig. 4a, fluorescence imaging revealed a signal that was easily visible around the area of injection, however low spatial resolution of this modality did not allow us to observe the intricate ductal tree network. Similar to the fluorescence imaging, the 2D or 3D MPI scans showed the presence of the contrast agent in the mice but proved difficult to identify the structure of ductal trees (Fig. 4b, c). In contrast to the other imaging modalities, the CT scans (both 2D and 3D) provided the capability to resolve the ductal tree network (Fig. 4d, e). Finally, PET/MR imaging of the ID injections of the agent chelated with Cu-64 (Fig. 5a-c), displayed a retention of the nanoparticle construct in the ductal tree network, localized to the mammary fat pad. PET signal generation from the site of injection could be traced in the 2D overlays of the slices and, when reconstructed in 3D, showed the wrapping of the ductal tree area from the front to the back of the animal (Supplemental Fig. 4, see ESM). Photoacoustic (Fig. 5d) images showed specific signal generation after bilateral ID injections, corroborating images obtained with other modalities. Accordingly, unilateral injections show no signal in the contralateral ductal tree supporting the authenticity of the signals (Supplemental Fig. 5, see ESM). The injections did not lead to any noticeable changes in animal's behavior or appearance of their internal organs upon euthanasia at the concentration tested. Histology of the ductal tree showed normal ductal epithelial cells (Fig. 5e, left), with accumulated agent as revealed by Cy5.5 fluorescence (Fig. 5e, middle and right). Cell morphology was unchanged, indicating the absence of tissue damage. Autoradiography performed on the excised fat pads of the mice which received ID injections showed that imaging was possible after as little as 5 minutes of exposure (Supplemental Fig. 6, see ESM).

Tumor model: In this model we performed imaging of labeled tumor cells injected in a fad pad of mice followed by multimodal imaging. Bioluminescence imaging identified two fad pads with luciferase-expressing cells (#3 and #8, Fig. 6a). Fluorescence imaging showed the signal originating from the omniparticle-labeled cells injected in the mammary fat pad 3# (Fig. 6b). Importantly, these cells were readily detectable by this imaging modality 5 days after injection in vivo and ex vivo (Supplemental Fig. 7a and b, see ESM) as confirmed by correlative fluorescence microscopy (Supplemental Fig. 7c, see ESM). Unlabeled cells (fat pad #8) were not detectable. MPI demonstrated a signal from fat pad #8 corresponding to about 130μg of iron (Fig. 6c). The signal was clearly detectable on CT as well as MR and PET images (Figs. 6d, e, f, g respectively). Detailed analysis of the line profiles on MR and PET images shows signal intensity along the blue crosshairs in the co-registered PET and MR image. Colocalization of negative signal in the MR scan and positive signal in the PET scan indicate the presence of the Cu-64 labeled nanoparticle in the lesion (Supplemental Fig. 8, see ESM). Photoacoustic images showed specific signal generation after injections of labeled cells, similar to the images obtained with other modalities (Fig. 6h). Ex vivo FL imaging showed generation of the signal from the injected labeled cells in the excised tissue (Fig. 6i). Correlative fluorescence microscopy demonstrated the presence of the omniparticle construct inside the labeled cells (Fig. 6j).

Discussion

The goal of this study was to create a novel contrast agent suitable for various imaging modalities that can bridge and strengthen the collaboration between the research fields as well as enrich the information obtained from any one modality. There are a multitude of imaging modalities being explored and used, as no one modality offers the solution to imaging challenges, with each having its own strengths and weaknesses. MRI and CT suffer from low sensitivity and often require high doses of contrast agents to enhance signal intensity which may be harmful for the patients (for example, gadolinium chelates) [3, 7]. PET and SPECT have high sensitivity but use harmful ionizing radiation (as does CT) and have low spatial resolution [6]. Optical imaging suffers from the depth limit of tissue penetration and the problems with autofluorescence in tissue [52]. Many researchers, ourselves included, have recently focused on developing multimodal imaging probes to integrate multiple imaging modalities into a single contrast agent to provide complementary information [8, 53–55]. The rationale for our study, therefore, was driven by the idea of an omniparticle contrast agent that could overcome individual weaknesses and provides a tool to co-register different modalities with a single agent, reducing variability in data interpretation created by co-registering different contrast agents used in different imaging techniques. Using a single agent removes the issue of co-administered agents having differing biodistribution and elimination kinetics and ensures the ability to image the region of interest with all desired modalities. It also eliminates the necessity for multiple injections, which is an important consideration in a clinical setting. More so, an omniparticle contrast would simplify and allow for the manual registration of different modalities from a single administration and work independently of, or with, artificial intelligence (A.I.) systems [56–57]. It could also provide a path towards establishing much needed standards within fields and eliminating variability between commercially available instruments. Importantly, with an all-in-one system, future therapeutic studies could be precisely monitored and quantitatively calculated for dose delivered vs the signal generated. Finally, bioengineering field could tremendously benefit from such agent where simple non-invasive referencing is needed to monitor the location of a surgical clamp [58–61] or a heart muscle patch [62–63].

Here we report on a multimodal – MPI, MRI, PA, FL, PET, CT – nanoparticle construct (termed omniparticle), its synthesis, characterization and functionality both *in vitro* and *in vivo*. The omniparticle showed intense signal generation with phantoms and sustained signal over multiple days of imaging experiments, both *in vitro* and *in vivo*. Even though the resolution of some imaging modalities did not allow for the full view of the ductal trees or injected cells, the agent was detected by all modalities. This is important for future applications where it can be used for passive or direct targeting after systemic administration considering an absence of toxicity. While not all readouts might be necessary for an individual in a clinical setting, our agent provides for this opportunity if necessary. Further development of an omniparticle contrast agent may also strengthen both the individual imaging modalities and the inter-field corroboration, thus improving the existing clinical modalities or aiding in the development of novel techniques. Importantly, as our particle is hydrophilic during synthesis and flexible for manipulation of functional groups with the dextran coating, we believe it makes an ideal candidate for future theranostics.

Conclusion

This study describes generation and testing of omniparticles intended for providing imaging contrast with multiple imaging modalities. In vitro and in vivo studies in two different animal models demonstrated robustness of the signal, absence of toxicity and persistence in cellular environment. We believe that this agent can be further developed for various disease settings such as cancer, diabetes, neurodegenerative and cardiovascular diseases.

Supplementary Material

Refer to Web version on PubMed Central for supplementary material.

Acknowledgements:

The authors would like to thank Gloria Perez for her assistance with autoradiography. The authors declare that they have no conflict of interest.

Funding:

This work was supported in part by R01 CA221771 and R01 CA261691 to A.M. and R21 CA226579 and R01 CA258314 to L.S.

References

1. Arami H, Teeman E, Troksa A, et al. (2017) Tomographic magnetic particle imaging of cancer targeted nanoparticles. Nanoscale 9:18723–18730.
2. de Vries EGE, Kist de Ruijter L, Lub-de Hooge MN, Dierckx RA, Elias SG, Oosting SF (2019) Integrating molecular nuclear imaging in clinical research to improve anticancer therapy. Nat Rev Clin Oncol 16:241–255. [PubMed: 30479378]
3. Kircher MF, de la Zerda A, Jokerst JV, et al. (2012) A brain tumor molecular imaging strategy using a new triple-modality MRI-photoacoustic-Raman nanoparticle. Nature medicine 18:829–834.
4. Maleszewski JJ, Anavekar NS, Moynihan TJ, Klarich KW (2017) Pathology, imaging, and treatment of cardiac tumours. Nat Rev Cardiol 14:536–549. [PubMed: 28436488]
5. Park SM, Aalipour A, Vermesh O, Yu JH, Gambhir SS (2017) Towards clinically translatable in vivo nanodiagnostics. Nat Rev Mater 2.
6. Signore A, Mather SJ, Piaggio G, Malviya G, Dierckx RA (2010) Molecular imaging of inflammation/infection: nuclear medicine and optical imaging agents and methods. Chem Rev 110:3112–3145. [PubMed: 20415479]
7. Smith BR, Gambhir SS (2017) Nanomaterials for In Vivo Imaging. Chem Rev 117:901–986. [PubMed: 28045253]
8. Yankeelov TE, Abramson RG, Quarles CC (2014) Quantitative multimodality imaging in cancer research and therapy. Nat Rev Clin Oncol 11:670–680. [PubMed: 25113842]
9. Yu EY, Bishop M, Zheng B, et al. (2017) Magnetic Particle Imaging: A Novel in Vivo Imaging Platform for Cancer Detection. Nano Lett 17:1648–1654. [PubMed: 28206771]
10. Lim S, Yoon HY, Jang HJ, et al. (2019) Dual-Modal Imaging-Guided Precise Tracking of Bioorthogonally Labeled Mesenchymal Stem Cells in Mouse Brain Stroke. ACS Nano 13:10991–11007.
11. Yu GT, Luo MY, Li H, et al. (2019) Molecular Targeting Nanoprobes with Non-Overlap Emission in the Second Near-Infrared Window for in Vivo Two-Color Colocalization of Immune Cells. ACS Nano 13:12830–12839.
12. Zheng B, Vazin T, Goodwill PW, et al. (2015) Magnetic Particle Imaging tracks the long-term fate of in vivo neural cell implants with high image contrast. Sci Rep 5:14055.

13. Grippin AJ, Wummer B, Wildes T, et al. (2019) Dendritic Cell-Activating Magnetic Nanoparticles Enable Early Prediction of Antitumor Response with Magnetic Resonance Imaging. ACS Nano 13:13884–13898.
14. Antoch G, Freudenberg LS, Beyer T, Bockisch A, Debatin JF (2004) To Enhance or Not to Enhance? 18F-FDG and CT Contrast Agents in Dual-Modality 18F-FDG PET/CT. J Nucl Med 45:56S–65S. [PubMed: 14736836]
15. Bae KT (2010) Intravenous contrast medium administration and scan timing at CT: considerations and approaches. Radiology 256:32–61. [PubMed: 20574084]
16. Seale MK, Catalano OA, Saini S, Hahn PF, Sahani DV (2009) Hepatobiliary-specific MR contrast agents: role in imaging the liver and biliary tree. Radiographics 29:1725–1748. [PubMed: 19959518]
17. Beckett KR, Moriarity AK, Langer JM (2015) Safe Use of Contrast Media: What the Radiologist Needs to Know. Radiographics 35:1738–1750. [PubMed: 26466182]
18. Bogdanov A Jr., Mazzanti ML (2011) Molecular magnetic resonance contrast agents for the detection of cancer: past and present. Semin Oncol 38:42–54. [PubMed: 21362515]
19. Pomara C, Pascale N, Maglietta F, Neri M, Riezzo I, Turillazzi E (2015) Use of contrast media in diagnostic imaging: medico-legal considerations. Radiol Med 120:802–809. [PubMed: 26082145]
20. Widmark JM (2007) Imaging-related medications: a class overview. Proc (Bayl Univ Med Cent) 20:408–417. [PubMed: 17948119]
21. Herfert K, Mannheim JG, Kuebler L, et al. (2020) Quantitative Rodent Brain Receptor Imaging. Mol Imaging Biol 22:223–244. [PubMed: 31168682]
22. Serkova NJ, Glunde K, Haney CR, et al. (2021) Preclinical Applications of Multi-Platform Imaging in Animal Models of Cancer. Cancer research 81:1189–1200. [PubMed: 33262127]
23. Weissleder R (2001) A clearer vision for in vivo imaging. Nature biotechnology 19:316–317.
24. Wahsner J, Gale EM, Rodriguez-Rodriguez A, Caravan P (2019) Chemistry of MRI Contrast Agents: Current Challenges and New Frontiers. Chem Rev 119:957–1057. [PubMed: 30350585]
25. Song G, Zheng X, Wang Y, Xia X, Chu S, Rao J (2019) A Magneto-Optical Nanoplatform for Multimodality Imaging of Tumors in Mice. ACS Nano 13:7750–7758. [PubMed: 31244043]
26. Kircher MF, Weissleder R, Josephson L (2004) A dual fluorochrome probe for imaging proteases. Bioconjug Chem 15:242–248. [PubMed: 15025519]
27. Townsend DW (2008) Dual-modality imaging: combining anatomy and function. J Nucl Med 49:938–955. [PubMed: 18483101]
28. Wang Y, Chen J, Yang B, et al. (2016) In vivo MR and Fluorescence Dual-modality Imaging of Atherosclerosis Characteristics in Mice Using Profilin-1 Targeted Magnetic Nanoparticles. Theranostics 6:272–286. [PubMed: 26877785]
29. Medarova Z, Pham W, Farrar C, Petkova V, Moore A (2007) In vivo imaging of siRNA delivery and silencing in tumors. Nature medicine 13:372–377.
30. Yigit MV, Ghosh SK, Kumar M, et al. (2013) Context-dependent differences in miR-10b breast oncogenesis can be targeted for the prevention and arrest of lymph node metastasis. Oncogene 32:1530–1538. [PubMed: 22580603]
31. Vogel P, Lother S, Ruckert MA, et al. (2014) MRI Meets MPI: a bimodal MPI-MRI tomograph. IEEE Trans Med Imaging 33:1954–1959. [PubMed: 25291350]
32. Vogel P, Markert J, Ruckert MA, et al. (2019) Magnetic Particle Imaging meets Computed Tomography: first simultaneous imaging. Sci Rep 9:12627.
33. Wang G, Chen C, Pai P, et al. (2019) Intraductal fulvestrant for therapy of ERalpha-positive ductal carcinoma in situ of the breast: a preclinical study. Carcinogenesis 40:903–913. [PubMed: 31046118]
34. Brock A, Krause S, Li H, et al. (2014) Silencing HoxA1 by intraductal injection of siRNA lipidoid nanoparticles prevents mammary tumor progression in mice. Sci Transl Med 6:217ra212.
35. Murata S, Kominsky SL, Vali M, et al. (2006) Ductal access for prevention and therapy of mammary tumors. Cancer research 66:638–645. [PubMed: 16423990]

36. Okugawa H, Yamamoto D, Uemura Y, et al. (2005) Effect of perductal paclitaxel exposure on the development of MNU-induced mammary carcinoma in female S-D rats. Breast cancer research and treatment 91:29–34. [PubMed: 15868429]
37. Sivaraman L, Gay J, Hilsenbeck SG, et al. (2002) Effect of selective ablation of proliferating mammary epithelial cells on MNU induced rat mammary tumorigenesis. Breast cancer research and treatment 73:75–83. [PubMed: 12083633]
38. Kenyon E, Westerhuis JJ, Volk M, et al. (2019) Ductal tree ablation by local delivery of ethanol prevents tumor formation in an aggressive mouse model of breast cancer. Breast Cancer Res 21:129. [PubMed: 31779648]
39. Stearns V, Mori T, Jacobs LK, et al. (2011) Preclinical and clinical evaluation of intraductally administered agents in early breast cancer. Sci Transl Med 3:106ra108.
40. Love SM, Zhang W, Gordon EJ, et al. (2013) A feasibility study of the intraductal administration of chemotherapy. Cancer Prev Res (Phila) 6:51–58. [PubMed: 23169924]
41. Chakravarty S, Hix JML, Wiewiora KA, et al. (2020) Tantalum oxide nanoparticles as versatile contrast agents for X-ray computed tomography. Nanoscale 12:7720–7734. [PubMed: 32211669]
42. Hoehn M, Wiedermann D, Justicia C, et al. (2007) Cell tracking using magnetic resonance imaging. J Physiol 584:25–30. [PubMed: 17690140]
43. Foster-Gareau P, Heyn C, Alejski A, Rutt BK (2003) Imaging single mammalian cells with a 1.5 T clinical MRI scanner. Magn Reson Med 49:968–971. [PubMed: 12704781]
44. Bulte JWM, Daldrup-Link HE (2018) Clinical Tracking of Cell Transfer and Cell Transplantation: Trials and Tribulations. Radiology 289:604–615. [PubMed: 30299232]
45. Krause S, Brock A, Ingber DE (2013) Intraductal injection for localized drug delivery to the mouse mammary gland. J Vis Exp.
46. Wang P, Yigit MV, Medarova Z, et al. (2011) Combined small interfering RNA therapy and in vivo magnetic resonance imaging in islet transplantation. Diabetes 60:565–571. [PubMed: 21270267]
47. Hifumi H, Yamaoka S, Tanimoto A, et al. (2009) Dextran Coated Gadolinium Phosphate Nanoparticles for Magnetic Resonance Tumor Imaging. Journal of Materials Chemistry 19:6393–6399.
48. Markides H, Rotherham M, El Haj AJ (2012) Biocompatibility and Toxicity of Magnetic Nanoparticles in Regenerative Medicine. Journal of Nanomaterials 2012:614094.
49. Yu M, Huang S, Yu KJ, Clyne AM (2012) Dextran and polymer polyethylene glycol (PEG) coating reduce both 5 and 30 nm iron oxide nanoparticle cytotoxicity in 2D and 3D cell culture. Int J Mol Sci 13:5554–5570. [PubMed: 22754315]
50. Yoo B, Ghosh SK, Kumar M, Moore A, Yigit MV, Medarova Z (2014) Design of nanodrugs for miRNA targeting in tumor cells. J Biomed Nanotechnol 10:1114–1122. [PubMed: 24749405]
51. Kumar M, Yigit M, Dai G, Moore A, Medarova Z (2010) Image-guided breast tumor therapy using a small interfering RNA nanodrug. Cancer research 70:7553–7561. [PubMed: 20702603]
52. Hong G, Antaris AL, Dai H (2017) Near-infrared fluorophores for biomedical imaging. Nature Biomedical Engineering 1:0010.
53. Laurent S, Forge D, Port M, et al. (2008) Magnetic iron oxide nanoparticles: synthesis, stabilization, vectorization, physicochemical characterizations, and biological applications. Chem Rev 108:2064–2110. [PubMed: 18543879]
54. Lemaster JE, Chen F, Kim T, Hariri A, Jokerst JV (2018) Development of a Trimodal Contrast Agent for Acoustic and Magnetic Particle Imaging of Stem Cells. ACS Applied Nano Materials 1:1321–1331. [PubMed: 33860154]
55. Wu L, Mendoza-Garcia A, Li Q, Sun S (2016) Organic Phase Syntheses of Magnetic Nanoparticles and Their Applications. Chem Rev 116:10473–10512.
56. Panayides AS, Amini A, Filipovic ND, et al. (2020) AI in Medical Imaging Informatics: Current Challenges and Future Directions. IEEE J Biomed Health Inform 24:1837–1857. [PubMed: 32609615]
57. Tang X (2020) The role of artificial intelligence in medical imaging research. BJR Open 2:20190031.

58. Van Praet KM, van Kampen A, Kofler M, et al. (2020) Minimally invasive surgical aortic valve replacement: The RALT approach. J Card Surg 35:2341–2346. [PubMed: 32643836]

59. Van Praet KM, Van Kampen A, Kofler M, et al. (2020) Minimally invasive surgical aortic valve replacement through a right anterolateral thoracotomy. Multimed Man Cardiothorac Surg 2020.

60. Li S, Zhang H, Chen M, Wang Z, Lin Y (2021) A multidisciplinary team nursing model in the treatment of patients undergoing transapical mitral valve clamping: a prospective study. J Cardiothorac Surg 16:203. [PubMed: 34321032]

61. Xue Y, Zhou Q, Li S, et al. (2021) Transapical Transcatheter Valve Replacement Using J-Valve for Aortic Valve Diseases. Ann Thorac Surg 112:1243–1249. [PubMed: 33248996]

62. Serpooshan V, Zhao M, Metzler SA, et al. (2013) The effect of bioengineered acellular collagen patch on cardiac remodeling and ventricular function post myocardial infarction. Biomaterials 34:9048–9055. [PubMed: 23992980]

63. Wei K, Serpooshan V, Hurtado C, et al. (2015) Epicardial FSTL1 reconstitution regenerates the adult mammalian heart. Nature 525:479–485. [PubMed: 26375005]

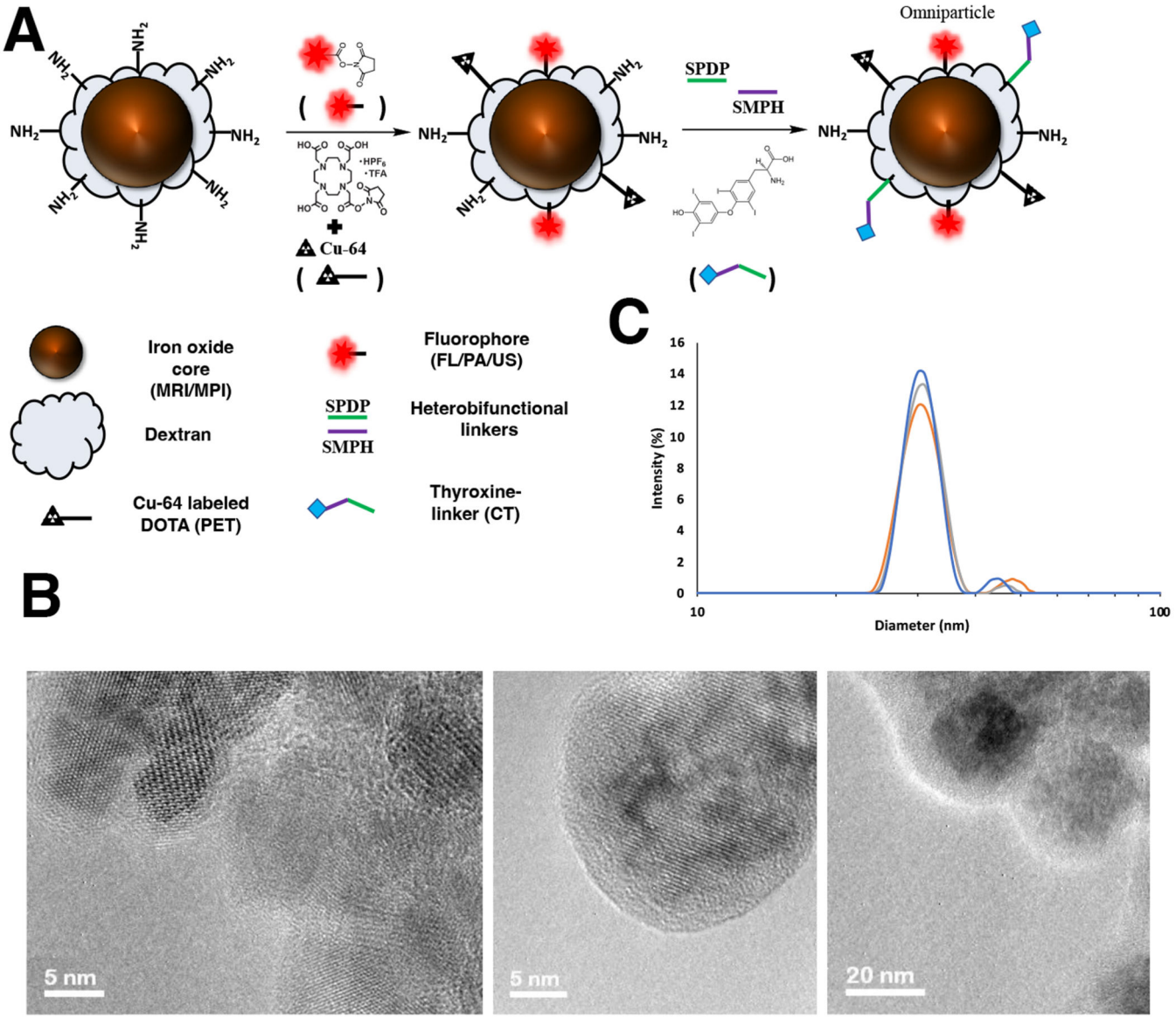

Figure 1.

Schematic representation of the omniparticle contrast agent with chemical functionalities. A) Transmission electron microscopy of the particle core and dextran coating prior to conjugation of the functional moieties. Particle cores averaged to between 15 and 20 nm with a sub 5 nm dextran coating. B) Average hydrodynamic diameter, as measured by dynamic light scattering, showed a major peak at approximate size of 30.67 +/− 1.53 nm (29.0 nm, orange; 32.0 nm, gray; 31.0 nm, blue) and an average zeta potential of +20.45 mV +/− 1.65 mV (18.714, 22.0147, 20.264).

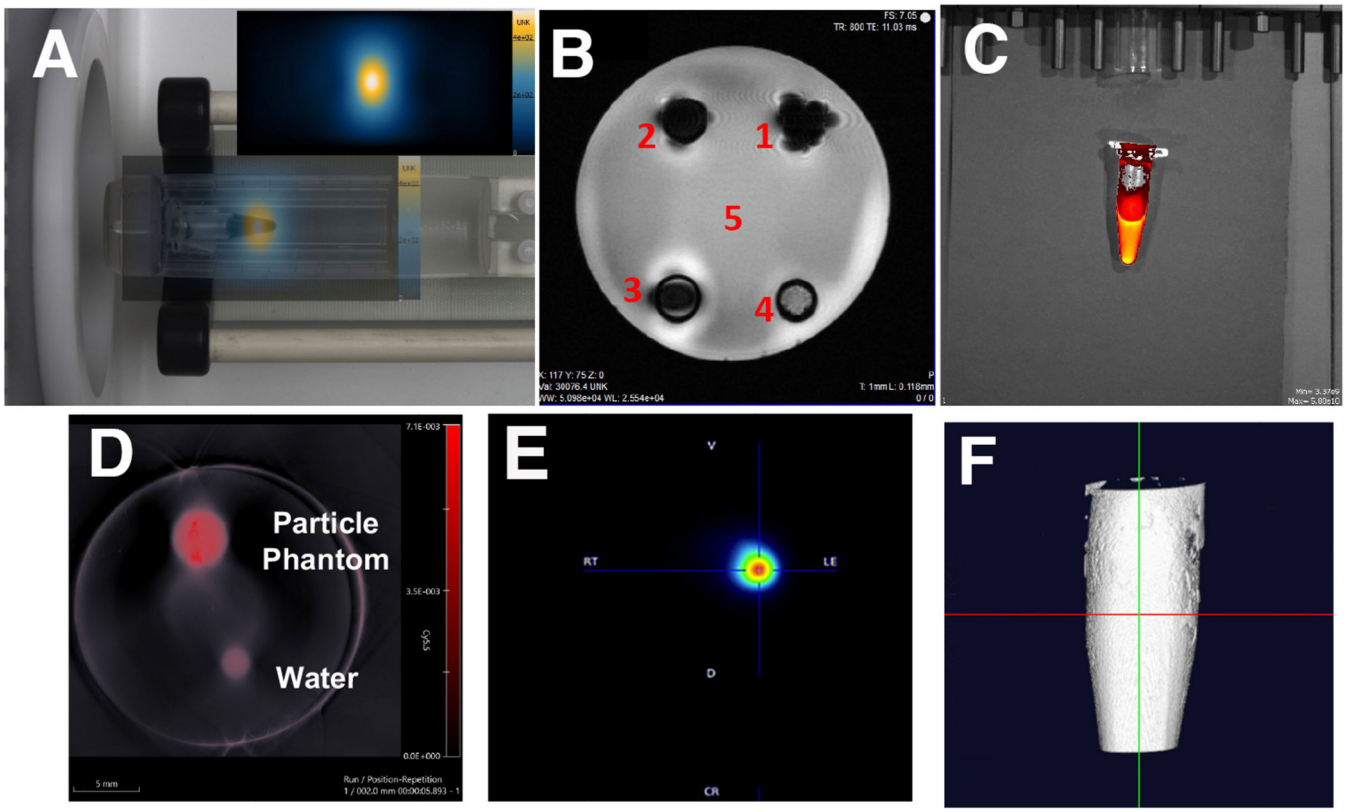

Figure 2.

Omniparticle contrast agent imaging capabilities. Phantoms showed imaged with A) Magnetic Particle Imaging (particle signal intensity (inset) overlaid with photo); B) Magnetic Resonance Imaging (1 – MNP core [30]; 2 – MNP core conjugated to Cy5.5; 3 – MNP core conjugated to Cy5.5 and thyroxine; 4 – completely oxidized nanoparticle core; 5 – water); C) Fluorescence imaging, D) Photoacoustic imaging, E) PET imaging and F) 3D computed tomography image afforded after T4 conjugation.

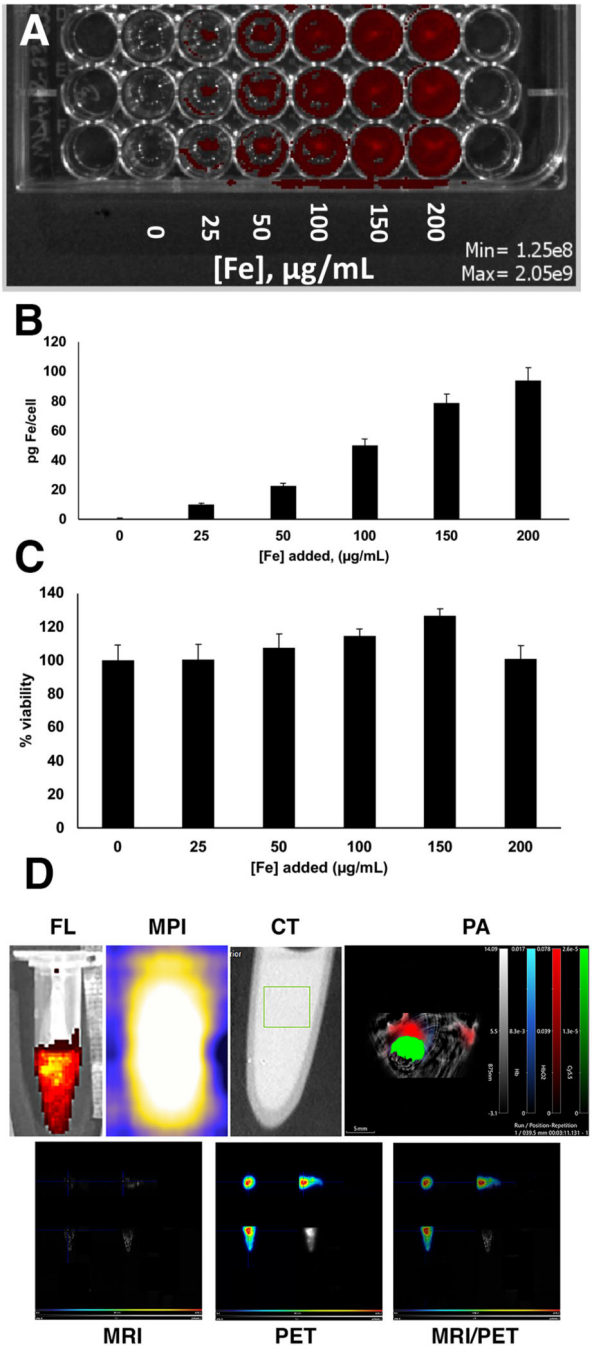

Figure 3.

In vitro studies of omniparticle contrast agent uptake and cellular viability in MDA-MB-231 cell line. A) Qualitative assessment of particle uptake as imaged with Cy5.5 fluorescence. B) Quantitative measurement of iron uptake in A. C) Cell viability upon incubation with the agent. D) Cell phantoms showing the presence of the agent after incubation with the cells with FL, MPI, CT, PA, MRI and PET. MRI/PET is also shown. MRI and PET images are showing (clockwise) axial, saggital and coronal view and maximum intensity projection.

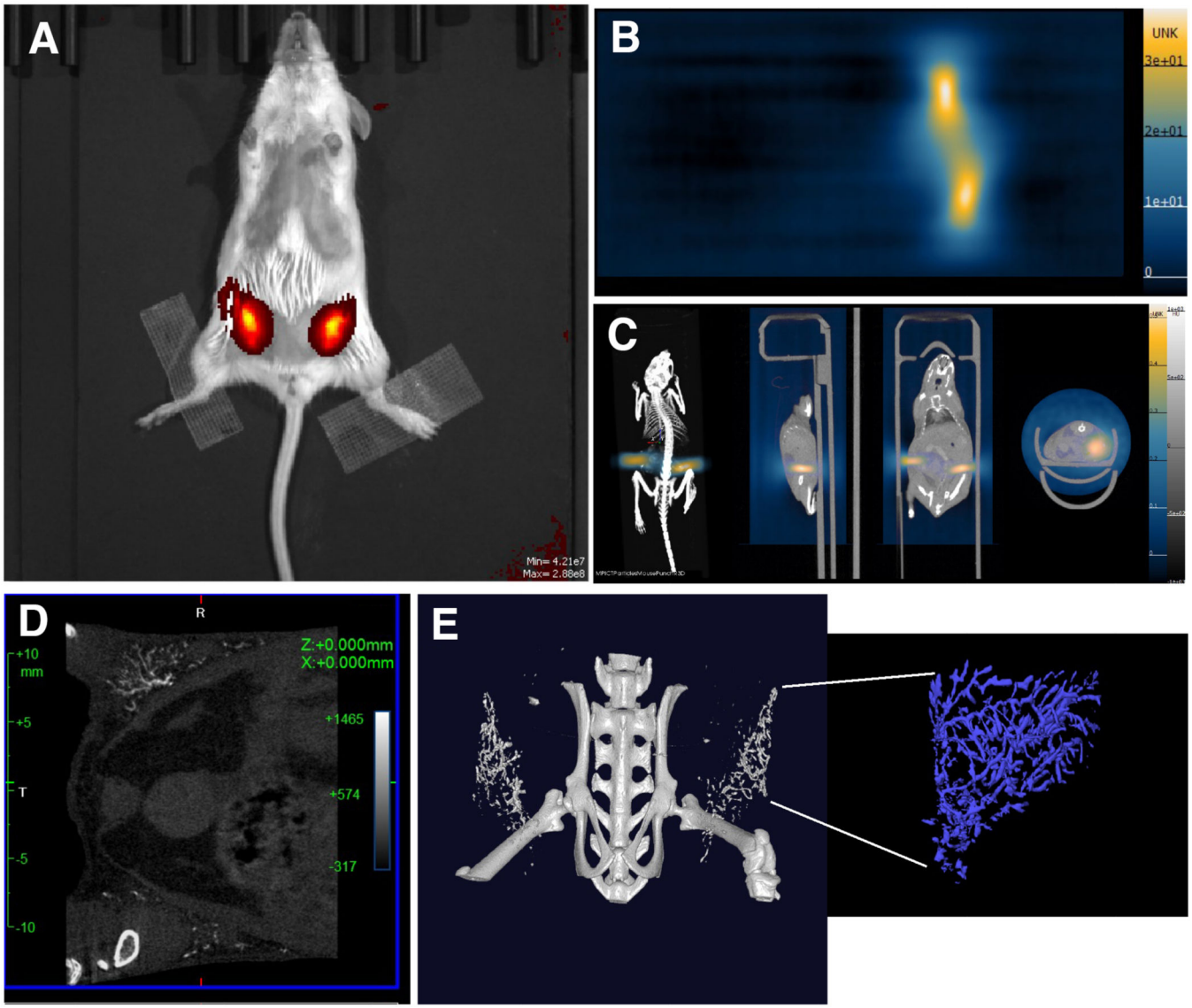

Figure 4.

Multimodal imaging of omniparticles after intraductal injection. A) Fluorescence imaging with the Cy5.5 fluorophore-labeled omnipartcles shows localization of the agent; B) 2D and C) 3D (overlayed with CT) MPI images showing signal generation due to the particle core. D) 2D and E) 3D CT images showing the intricate detail of the ductal tree network (blue color is optimized for visualization of ductal tree).

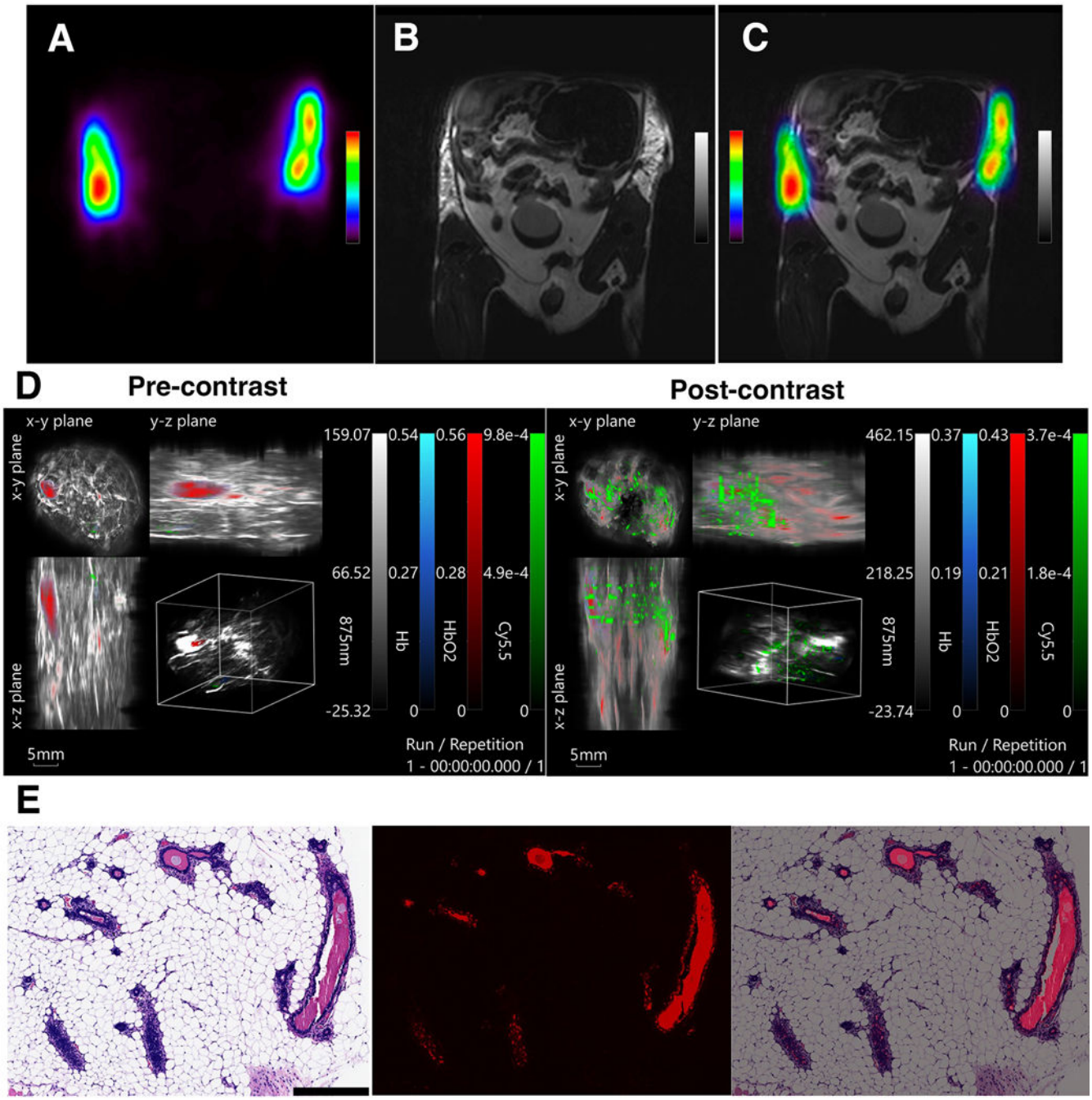

Figure 5.

In vivo imaging of intraductal injections of the fully conjugated contrast agent, radiolabeled with Cu-64, imaged with A) PET and B) MRI, and the C) overlay of the two modalities. D) Photoacoustic imaging (left – pre-contrast; right – post-contrast). E) Histology of the excised ductal tree tissue. Left: H&E stain of the ductal epithelial cells after injection with the contrast agent. Middle: Fluorescence of the agent accumulated in the ductal epithelial cells, imaged in Cy5.5 channel; Right: the merged images.

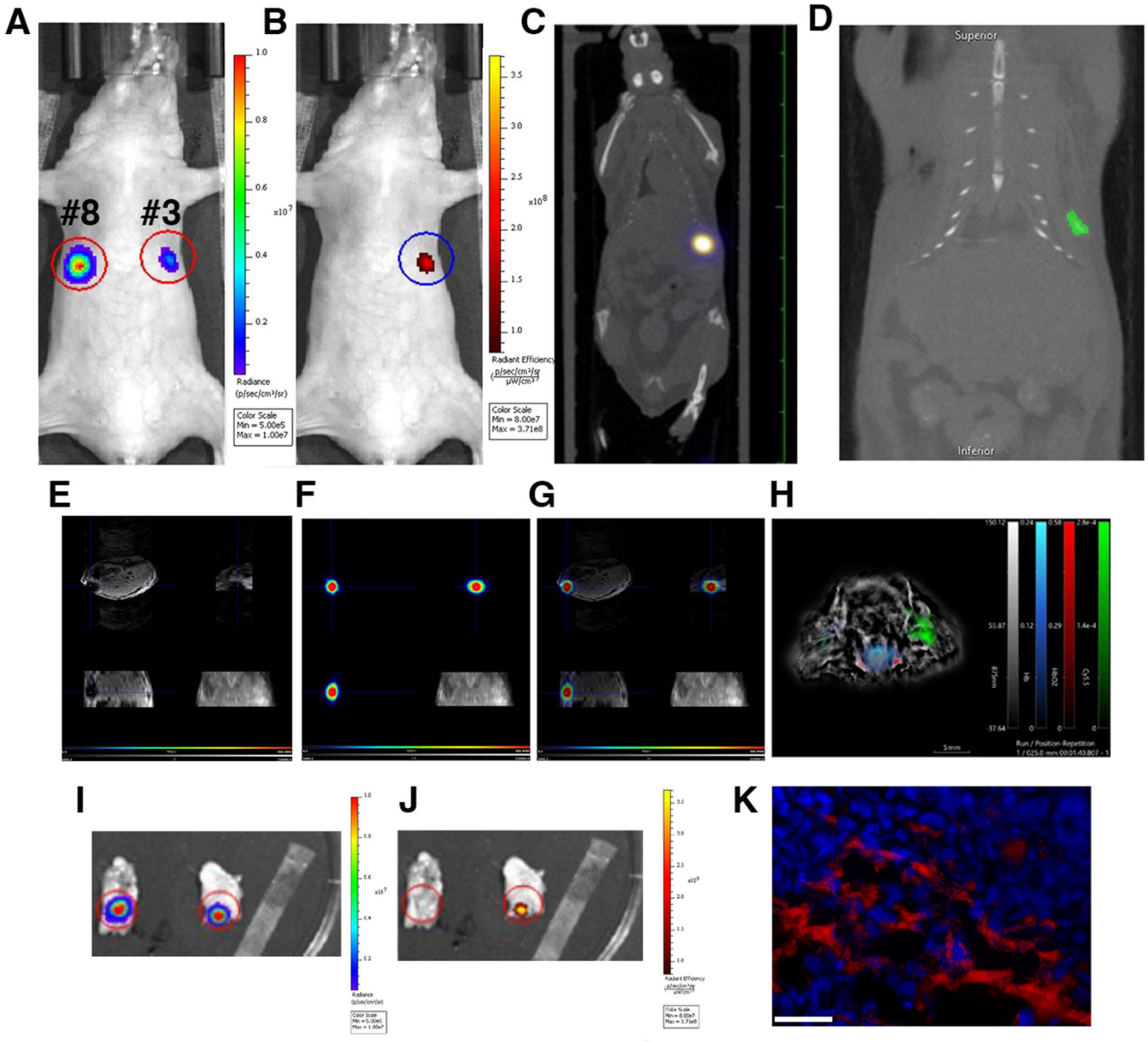

Figure 6.

In vivo imaging of labeled tumor cells injected in the mammary fat pad. A) In vivo bioluminescence imaging of the cells injected in mammary fat pads #3 and #8. B) In vivo fluorescence imaging showing the presence of the labeled cells in the mammary fat pad #3. C) In vivo MPI demonstrating the presence of the signal. D) 2D CT demonstrates the presence of the labeled cells. E) In vivo MRI images showing signal generation due to the presence of the particle core in labeled cells. F) In vivo PET imaging. G) Merged MRI and PET. MRI and PET images are showing (clockwise) axial, saggital and coronal view and maximum intensity projection. H). Optoacoustic imaging showing generation of the signal in the fat pad injected with labeled cells. I) Ex vivo BLI imaging and J) FL imaging (right) of the excised tissue showing generation of the signal from the injected labeled cells.

K) Correlative fluorescence microscopy demonstrating the presence of the omniparticle construct inside the labeled tumor cells. Bar=50μm.